iScience

CellPress
OPEN ACCESS

Article

Rapid and label-free histological imaging of unprocessed surgical tissues via dark-field reflectance ultraviolet microscopy

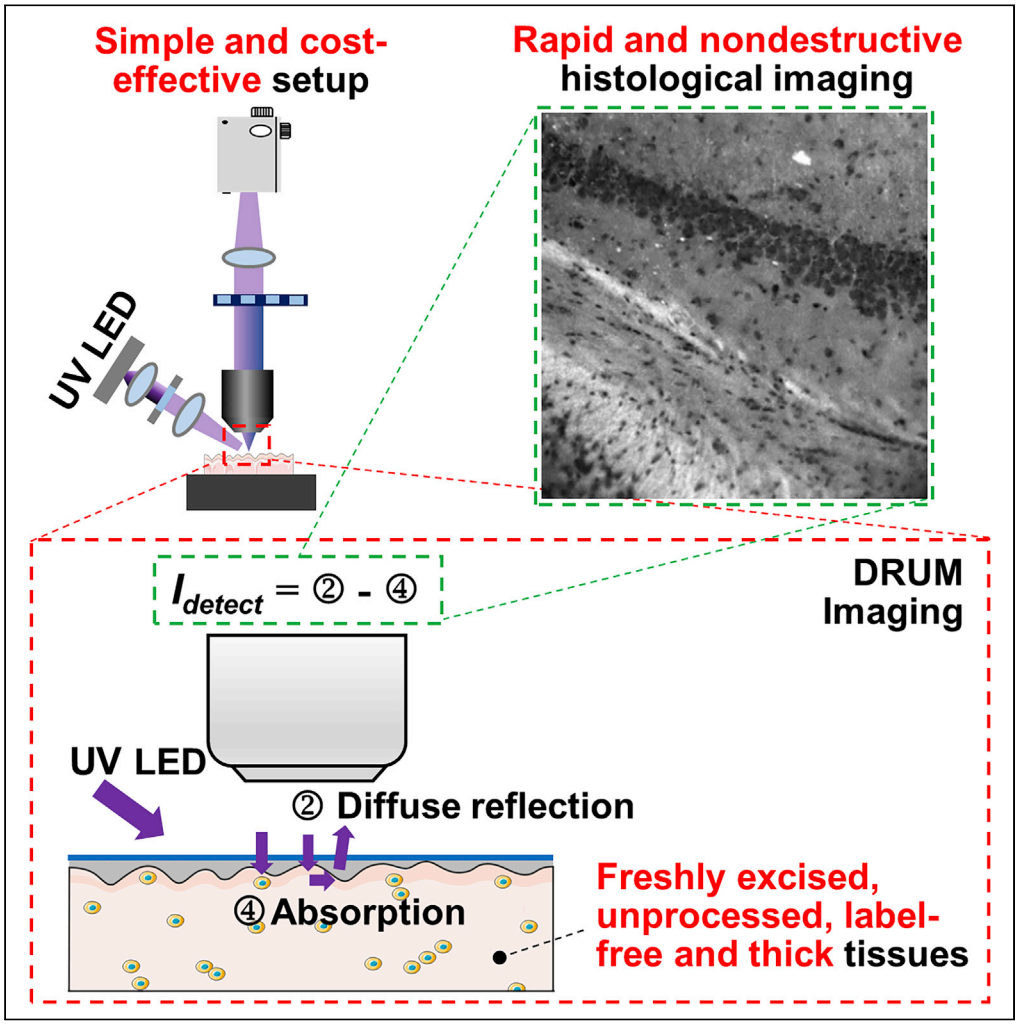

Shiwei Ye, Junjie Zou, Chenming Huang, ..., Lili Niu, Peng Gong, Wei Zheng

zhengwei@siat.ac.cn

Highlights

DRUM enables label-free histological imaging with the shortest turnaround time

The visibility of cell nuclei by DRUM is close to the degree of labeled images

DRUM reveals diagnostic features comparable with the standard H&E images

DRUM is non-destructive and is compatible with routine pathological examinations

Ye et al., iScience 26, 105849
January 20, 2023
https://doi.org/10.1016/j.isci.2022.105849

iScience

CellPress
OPEN ACCESS

Article

Rapid and label-free histological imaging of unprocessed surgical tissues via dark-field reflectance ultraviolet microscopy

Shiwei Ye,[1,2,9] Junjie Zou,[3,9] Chenming Huang,[1,2] Feng Xiang,[1,2] Zonghua Wen,[4] Nannan Wang,[1,2] Jia Yu,[1,2] Yuezhi He,[1,2] Peng Liu,[5] Xin Mei,[6] Hui Li,[1,2] Lili Niu,[3] Peng Gong,[7,8] and Wei Zheng[1,2,10,*]

SUMMARY

Routine examination for intraoperative histopathologic assessment is lengthy and laborious. Here, we present the dark-field reflectance ultraviolet microscopy (DRUM) that enables label-free imaging of unprocessed and thick tissues with subcellular resolution and a high signal-to-background ratio. To the best of our knowledge, DRUM provides image results for pathological assessment with the shortest turnaround time (2-3 min in total from sample preparation to tissue imaging). We also proposed a virtual staining process to convert DRUM images into pseudo-colorized images and enhance the image familiarity of pathologists. By imaging various tissues, we found DRUM can resolve cell nuclei and some extranuclear features, which are comparable to standard H&E images. Furthermore, the essential diagnostic features of intraoperatively excised tumor tissues also can be revealed by DRUM, demonstrating its potential as an additional aid for intraoperative histopathology.

INTRODUCTION

Intraoperative histopathology is essential for surgical margin assessment and is used to examine whether the tumor is completely excised.[1] Routine pathological examination was performed by the microscopic examination of tissues that were formalin-fixed and paraffin-embedded (FFPE), thinly sectioned, and stained. This is a lengthy and laborious process that fails to intraoperatively guide surgeons. Preparing frozen tissues is a more rapid alternative, but it still requires a turnaround time of ~30 min. Furthermore, freezing artifacts caused by edematous and fatty tissues affect histopathological interpretation and diagnostic accuracy.[2] In addition, because of the destructive nature of FFPE histology and frozen sectioning, a large number of excised tissues may be wasted, compromising their value in downstream molecular and genetic analyses. Therefore, the development of a rapid and nondestructive tissue assessment tool can assist in intraoperative decision-making, minimize physical and mental patient suffering, and reduce surgical risk.

Advanced optical imaging techniques have demonstrated significant success in pathological tissue assessment over the past few decades. Replacing the physical section of FFPE or frozen tissues with an optical section can significantly simplify the sample preparation procedure. Microscopy with ultraviolet surface excitation (MUSE) uses the shallow penetration depth of ultraviolet light to achieve moderate optical sectioning.[3–5] Structured illumination microscopy (SIM) rejects out-of-focus background digitally by leveraging the fact that only in-focus components can be modulated by structured illumination.[6–8] Light-sheet microscopy (LSM) achieves optical sectioning by a thin "selective" illumination plane and the signal collection from the orthogonal direction.[9–12] Although these technologies can be applied to the pathological assessment of thick tissues and shorten turnaround time, fluorescence labeling is still required to provide image contrast. Fluorescence labeling is challenging to be integrated into the current clinical practice, especially intraoperative pathological examination. Thus, label-free imaging based on endogenous contrast mechanisms is highly desired in modern clinical settings. Reflectance confocal microscopy (RCM) utilizes the refractive properties of various components, including melanin, keratin, and collagen, and exhibits superiority in dermatology.[13–15] The contrast in ultraviolet photoacoustic microscopy (UV-PAM) arises from intrinsic light absorption, which enables high-contrast imaging of cell nuclei.[16–18] Nonlinear microscopy, including multiphoton microscopy and stimulated Raman scattering microscopy, can generate optical signals from different sources, such as autofluorescence emission,[19–21]

[1]Research Center for Biomedical Optics and Molecular Imaging, Shenzhen Key Laboratory for Molecular Imaging, Guangdong Provincial Key Laboratory of Biomedical Optical Imaging Technology, Shenzhen Institute of Advanced Technology, Chinese Academy of Sciences, Shenzhen 518055, China

[2]CAS Key Laboratory of Health Informatics, Shenzhen Institutes of Advanced Technology, Chinese Academy of Sciences, Shenzhen 518055, China

[3]Paul C. Lauterbur Research Center for Biomedical Imaging, Shenzhen Institutes of Advanced Technology, Chinese Academy of Sciences, Shenzhen 518055, China

[4]Department of Pathology, Shenzhen University General Hospital, Shenzhen 518055, China

[5]Department of General Surgery, Shenzhen University General Hospital & Carson International Cancer Center, Shenzhen University, Shenzhen 518055, China

[6]Department of Neurosurgery, Sun Yat-sen Memorial Hospital, Guangzhou 510235, China

[7]Department of General Surgery & Institute of Precision Diagnosis and Treatment of Gastrointestinal Tumors, Shenzhen University General Hospital & Shenzhen University Clinical Medical Academy, Shenzhen 518055, China

[8]Carson International Cancer Center & Guangdong Provincial Key Laboratory of Regional Immunity and Diseases, Shenzhen University Health Science

Continued

noncentrosymmetric structures,[22,23] tissue interfaces with a change in refractive indices,[24,25] and molecular vibrations.[26–28] However, these scanning-based methods have limited imaging throughput and cannot meet the requirements for rapid pathological tissue assessment. Furthermore, the need for bulky and expensive lasers for UV-PAM or NLM increases the total facility budget and is a challenge for the cost-sensitive field of pathology. Full-field optical coherence tomography (FF-OCT) can detect the back-reflected light from structures with different refractive indices and enables parallel detection of 2D label-free images without scanning.[29–31] However, FF-OCT is not typically designed to achieve subcellular resolution and cannot visualize cell nuclei, which are important diagnostic features.

Here, we present a rapid, nondestructive, and cost-effective histological imaging method called dark-field reflectance ultraviolet microscopy (DRUM). By using the endogenous mechanisms of both reflectance and absorption, DRUM enables label-free imaging of unprocessed and thick tissues with subcellular resolution and high signal-to-background ratio (SBR). To the best of our knowledge, DRUM can provide the image results for pathological assessment with the shortest turnaround time (2-3 min in total from sample preparation to tissue imaging). Furthermore, a virtual staining process was proposed to convert DRUM images into pseudo-colorized images (pseudo-colorized DRUM) and enhance the image familiarity of the pathologists. The capacity of DRUM was verified by imaging various tissues, including mouse brain and spleen tissues, human brain tumor tissues, and human breast cancer tissues. The results suggest that the proposed method can not only rapidly provide tissue architecture and subcellular features similar to conventional pathological images but also accurately differentiate between normal and tumor tissues.

RESULTS

Histological imaging by dark-field reflectance ultraviolet microscopy

DRUM enables histological imaging by leveraging two endogenous contrast mechanisms. First, nucleic acids have strong absorption characteristics in the deep-ultraviolet (deep-UV) light range, which can be used to provide a negative contrast of cell nuclei.[32] Especially, 260-nm deep-UV light corresponds to the absorption peak of nucleic acids[32–34] and is used in the DRUM system to maximize the negative signal of cell nuclei. Second, some extranuclear components, such as cytoplasm, keratin, and collagen, strongly reflect 260-nm deep-UV light and appear bright in DRUM images. Furthermore, the difference in refractive index (RI) of various extranuclear components causes the recognition of some tissue features.[35,36]

However, these two endogenous signals cannot be directly collected using conventional reflected light microscopy (RLM) with UV excitation. In the RLM, the reflected signals include specular reflection, diffuse reflection from tissues, and scattered light from tissue interfaces (Figure 1A).[37,38] In general, specular reflection is the dominant source in a bright-field configuration, and details from the tissues are almost invisible (Figure 1C). Thus, our DRUM microscope employs dark-field illumination to eliminate the background of specular reflection. However, even in the dark-field configuration, the collected signals primarily originate from the scattered light from the tissue interfaces and cannot reveal the cell nuclei (Figure 1D). To relieve the influence of the scattered light, DRUM further filled the space between the coverslip and tissue interfaces with a liquid to match the RI. In this study, phosphate-buffered saline (PBS) or glycerinum was chosen as the filling liquid, which has an RI similar to that of biological tissues[35,36,39] and shows great biocompatibility. In other words, the image contrast of DRUM arises from two aspects: the absorption of cell nuclei towards deep-UV light and diffuse reflection, which has been multiply scattered by extranuclear components within tissues (Figure 1B). By fully utilizing the two label-free contrast mechanisms, DRUM can not only resolve cell nuclei with high visibility but also provide rich information on extranuclear features (Figure 1E).

As depicted in Figure 1F, our DRUM microscope uses UV light-emitting diodes (LEDs) and a set of bandpass filters to tune the imaging wavelength. Here, we use three filters with central wavelengths at 260, 357, and 447 nm. The three filters in the collecting path indicate DRUM images (I_{260}), autofluorescence images (I_{357}), and fluorescence images (I_{447}) stained with 4′,6-diamidino-2-phenylindole (DAPI), respectively. It has been reported that the autofluorescence of UV excitation is dominated by tryptophan, which has an emission peak at 357 nm. Other UV fluorescents, such as amino acids, tyrosine, and phenylalanine, are often quenched by tryptophan.[40] In this study, DRUM images only require a frame of I_{260} without post-processing, whereas both I_{260} and I_{357} are used to form a pseudo-colorized DRUM image (Figure 1G, see method details). I_{447} is an important verification for cell nuclei imaging and provides a comparison with DRUM images. It is noted that, to remove artifacts from non-uniform illumination, the collected images were

Center, Shenzhen 518055, China

[9]These authors contributed equally

[10]Lead contact

*Correspondence: zhengwei@siat.ac.cn

https://doi.org/10.1016/j.isci.2022.105849

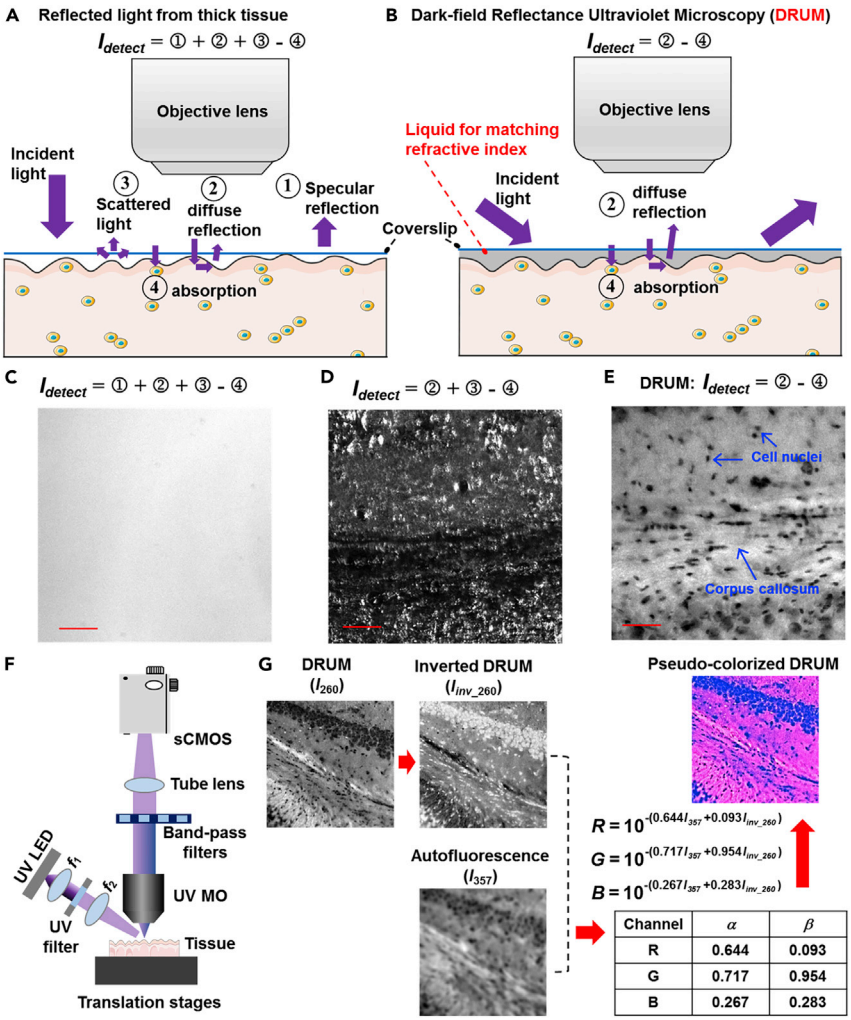

Figure 1. Histological imaging by DRUM and pseudo-colorized DRUM

(A) Reflected light from thick tissues in RLM.

(B) Principle of DRUM.

(C–E) The imaging of the same mouse brain tissues by bright-field RLM, dark-field RLM, and DRUM.

(F) Schematic of the DRUM system.

(G) Diagram showing the steps to obtain the pseudo-colorized DRUM images. I_{260}, DRUM images; I_{inv_260}, inverted DRUM images; I_{357}, autofluorescence images, scale bars: 50 μm (C–E).

normalized to a reference background image acquired from a blank area on the sample for each wavelength. In addition, the image acquisition in different filter channels requires slight axial adjustment for re-focusing. Because the DRUM microscope is simple and it has relatively small chromatic aberration. As a result, the collection of both I_{260} and I_{357} will not significantly increase the turnaround time for pseudo-colorized DRUM images (see the last section of Results).

Dark-field reflectance ultraviolet microscopy imaging with thin and label-free mouse brain slices

First, we validated the performance of DRUM by imaging label-free thin mouse brain slices. One excised mouse brain was manually cut into two halves at the coronal plane at a distance of −1.94 mm from bregma. One half was processed into frozen tissues and sectioned at a thickness of ~10 μm, and the thin frozen slices were imaged using DRUM. Because no exogenous components are introduced during frozen slice preparation, frozen thin slices are suitable for the preliminary validation of label-free DRUM imaging. The other half was histologically processed to obtain the corresponding H&E-stained images for

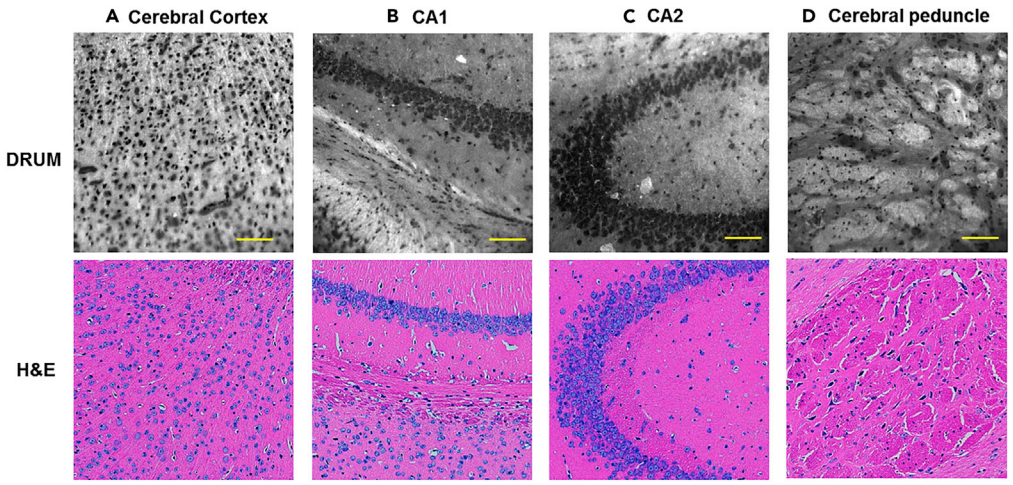

Figure 2. DRUM images and comparison with histological H&E imaging of thin mouse brain tissue slices

(A) Cerebral cortex.

(B) Field CA1 of hippocampus.

(C) Field CA2 of hippocampus.

(D) Cerebral peduncle. Scale bars: 100 μm (A-D).

comparison purposes. As shown in Figure 2, cell nuclei distributed in different regions of the mouse brain were revealed with negative contrast in the DRUM images. In particular, the densely packed cell nuclei in CA1 and CA2 of the hippocampus (CA1 and CA2) (Figures 2B and 2C) can be resolved individually. Other anatomical structures, such as the corpus callosum (Figure 2B) and cerebral peduncle (Figure 2D), were also well recognized because of RI differences.[41] Multiple similarities can be found in the DRUM and H&E-stained images. However, similar to other UV-based imaging methods,[16,19] it is still difficult to resolve nucleoli using DRUM.

Dark-field reflectance ultraviolet microscopy imaging of freshly excised, unprocessed, and thick tissues

To demonstrate the imaging capacity of thick and label-free tissues by DRUM and pseudo-colorized DRUM, freshly excised mouse brains and spleens were manually sectioned at a thickness of ~1.5 mm using a scalpel and then imaged by DRUM. In addition, to obtain the pseudo-colorized DRUM, the corresponding autofluorescence images from the same area were captured by changing the filter wheel into a 357-nm filter channel. Subsequently, the tissues were processed using a standard histological procedure to obtain H&E-stained images for comparison. Figure 3A shows the imaging results of one whole coronal plane of the mouse brain, while two zoomed-in DRUM images are shown in Figure 3B. Even in freshly excised, thick, and label-free tissues, cell nuclei and some anatomical structures, such as the caudoputamen, internal capsule, hippocampus, corpus callosum, and ventricle, were resolved. Furthermore, we magnified four ROIs (indicated as blue, yellow, red, and brown solid boxes in Figure 3B) with the corresponding pseudo-colorized DRUM and H&E images in Figures 3C–3F. The pseudo-colorized DRUM images can closely approximate the authentic H&E appearance and thus enhance the image familiarity of the pathologists. Similarly, cell nuclei distributed in the cortex of the mouse spleen were well recognized by DRUM, as shown in Figures 3G–3I. The corresponding pseudo-colorized DRUM and H&E images are also presented, and a similar density degree of cell nuclei is observed. Note that the microtome sectioned FFPE thin slice cannot exactly replicate the surface imaged by DRUM owing to tissue deformation and the difference in imaging thickness. Despite this difference, the structural features were remarkably similar. Furthermore, the turnaround time of the proposed method is only 2-3 min, including 1-2 min for thick-tissues preparation, ~300 ms for each image acquisition, and ~0.5 s for virtual staining. Even for extended-FOV imaging, the total turnaround time is still a few minutes, owing to the fast imaging ability of wide-field DRUM configuration. In addition, a cover glass was used to flatten the tissue surface as much as possible, then no refocusing is needed during the extended-FOV imaging process. The synchronous control of the UV sCMOS camera and the 3-axis motorized stage was also performed to minimize the time cost of extended-FOV imaging.

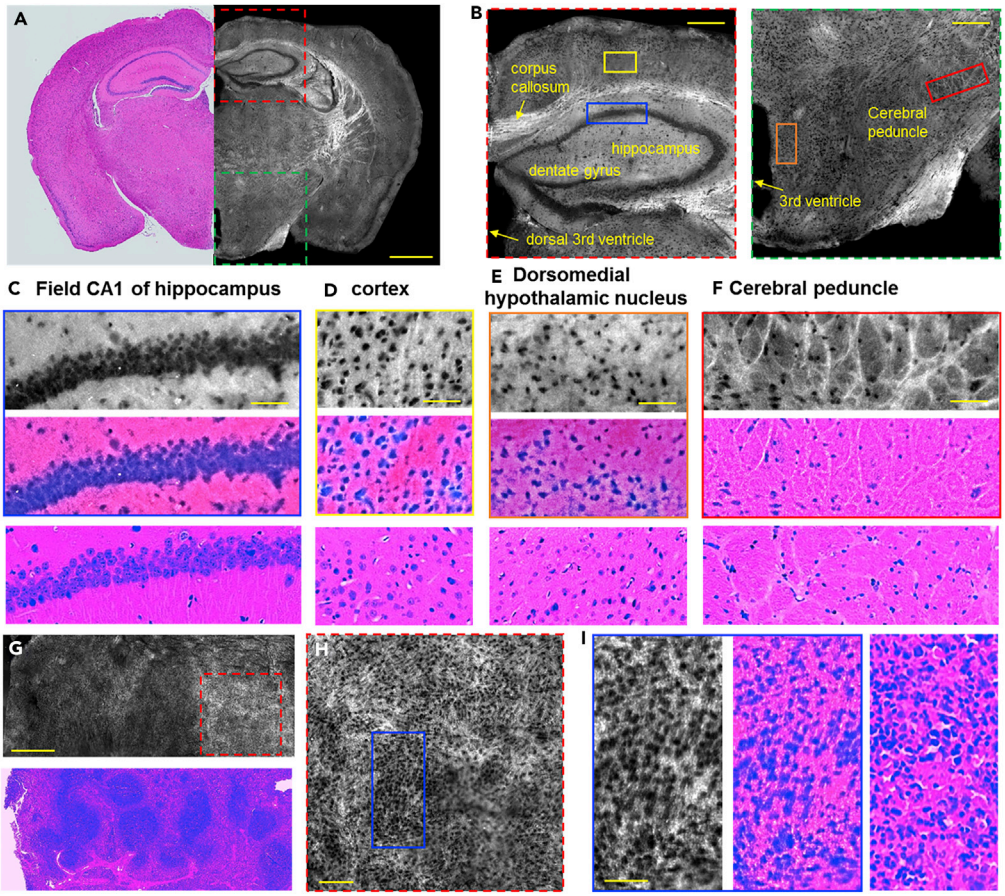

Figure 3. Validation of DRUM and pseudo-colorized DRUM with freshly excised, thick, and label-free mouse brain/spleen tissues

(A) Combination of extended-FOV DRUM images and H&E images of a mouse brain.

(B) Zoomed-in DRUM images of red and green dashed regions in (A), respectively.

(C–F) Zoomed-in DRUM images (top) of blue, yellow, orange, and red solid regions in (B), with the corresponding pseudo-colorized DRUM images (middle) and H&E images (bottom).

(G) Extended-FOV DRUM image and H&E image of a mouse spleen.

(H) Zoomed-in DRUM image of red dashed region in (A).

(I) Zoomed-in DRUM image (left) of the blue solid region in (H), with the corresponding pseudo-colorized DRUM image (middle) and H&E image (right). Scale bars: 1 mm (A), 300 μm (B), 50 μm (C–F, I), 500 μm (G), 100 μm (H).

Dark-field reflectance ultraviolet microscopy imaging of freshly excised and thick mouse brain-tumor tissues

Glioblastoma (GBM) is among the most invasive and lethal cancers, frequently infiltrating the surrounding healthy tissue and resulting in rapid recurrence.[42,43] Intraoperative histopathology is essential for the accurate demarcation of glioblastoma. Here, the feasibility of DRUM and pseudo-colorized DRUM in clinical applications was verified by imaging GL261 tumor-bearing mouse brain tissues. Freshly excised and thick tissues were obtained 14 days after tumor cell implantation. After DRUM imaging, the specimens were histologically processed to obtain H&E-stained images for comparison. Figure 4A depicts an extended-FOV DRUM image, whereas two zoomed-in DRUM images with the corresponding H&E images are presented in Figures 4B and 4C. Similar to the H&E image, a cluster of dense cell nuclei was surrounded by bright extranuclear features in the DRUM image (Figure 4B), which was diagnosed as a marginal invasion of the tumor by one pathology (Z. Wen). Furthermore, the tumors were clearly established and highly proliferative in the lower region of Figure 4A, and both the DRUM and H&E images outline a clear boundary between the normal and tumor regions (Figure 4C). The ROIs (indicated as blue and green solid boxes in Figure 4C) from the normal and tumor regions, respectively, are magnified with the corresponding pseudo-colorized DRUM and H&E images in Figures 4D and 4E. Similar to the conventional H&E results, the tumor region in

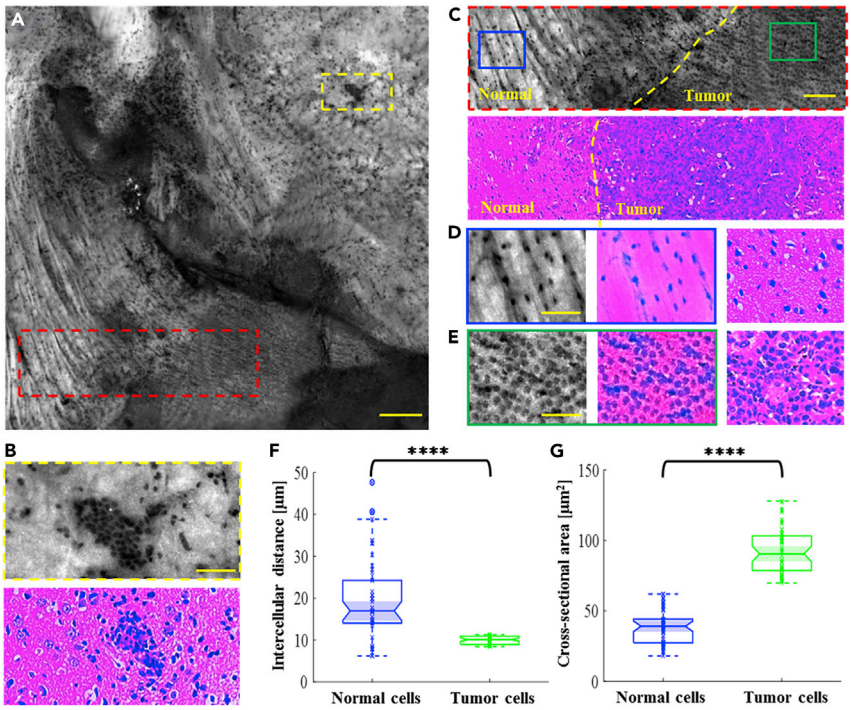

Figure 4. DRUM and pseudo-colorized DRUM validation of freshly excised and thick mouse brain-tumor tissues

(A) Extended-FOV DRUM image.

(B and C) Zoomed-in DRUM images of yellow and red dashed regions in (A), with the corresponding H&E images.

(D and E) Zoomed-in DRUM images (left) of blue and green solid regions in (C), with the corresponding pseudo-colorized DRUM images (middle) and H&E images (right).

(F and G) Distributions of intercellular distances and nuclear cross-sectional areas of normal and tumor cells derived from (C) (N = 50). Scale bars: 200 μm (A), 100 μm (C), 50 μm (B, D, and E). ****: $p < 0.00001$, and the significance is defined as $p < 0.05$.

DRUM and pseudo-colorized DRUM showed a high density of cell nuclei and was immediately adjacent to the normal tissue with low cellularity.

To analyze the nuclear features, the cross-sectional area and intercellular distance of cell nuclei, which play an important role in tissue phenotyping and histologic tumor grading, were extracted for the quantitative comparison between normal and tumor regions. To calculate these two parameters, DRUM images were segmented using a Fiji plugin[44] (trainable Weka segmentation[45]) and subsequently converted to a binary image (see method details). With the localized center positions of the cell nuclei, the intercellular distance is calculated as the shortest adjacent distance to a neighboring cell nucleus. Figures 4F and 4G show the statistical results, which were calculated from 50 cell nuclei in the two regions of Figure 4C. The median values of intercellular distance were 16.97 μm for normal cells and 10.1 μm for tumor cells, while the median values of the cross-sectional area were 39.05 μm^2 for normal cells and 90.47 μm^2 for tumor cells. This indicates that tumor cells and normal cells can be distinguished based on nuclear features.

Dark-field reflectance ultraviolet microscopy imaging of intraoperatively excised human tumor tissues

To further demonstrate the capacity of DRUM and pseudo-colorized DRUM in an intraoperative setting, formalin-fixed and thick human brain tumor tissues were imaged using the corresponding H&E-stained images as a reference. The specimen from the patient was pathologically confirmed as a meningioma. An extended FOV DRUM image with the corresponding H&E image under the same magnification is shown in Figure 5A. Evidently, lobules of tumorous cells are demarcated by collagen-rich bundles, which is typical for meningiomas. One region in Figure 5A (indicated by the green dashed box) is magnified in Figure 5B, where a cluster of tumor cell nuclei can be clearly observed. Furthermore, Figures 5C and 5D show two

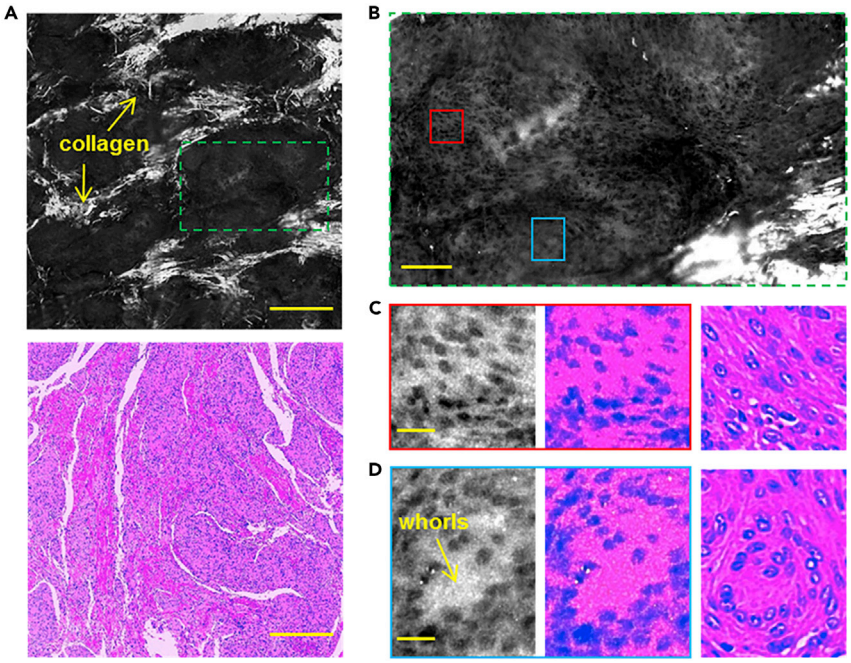

Figure 5. DRUM and pseudo-colorized DRUM validation of formalin fixed and thick human brain-tumor tissues

(A) Extended-FOV DRUM image and H&E image.

(B) Zoomed-in DRUM image of green dashed regions in (A).

(C and D) Zoomed-in DRUM images (left) of red and blue solid regions in (B), with the corresponding pseudo-colorized DRUM images (middle) and H&E images (right). The contrast of DRUM images was adjusted in Fiji. Scale bars: 400 μm (A), 100 μm (B), 20 μm (C and D).

zoomed-in DRUM images (indicated by red and blue solid boxes in Figure 5B) with pseudo-colorized DRUM and H&E images. Similar to the H&E images, DRUM and pseudo-colorized DRUM revealed the histopathological features of meningiomas, such as the whorled architecture (Figure 5D). DRUM has the potential to assist in the diagnosis of tumors and differentiate the subtypes of brain tumors (Figure S1 presents the results of another human brain tumor tissues).

Finally, the surgically excised, cryopreserved, and thick human breast cancer tissues were imaged to demonstrate the effectiveness of DRUM and pseudo-colorized DRUM. Over 20% of patients with breast cancer treated with breast-conserving surgery (BCS) undergo repeated surgeries.[46,47] Hence, a rapid and accurate tissue imaging method for the intraoperative assessment of BCS is required. Two DRUM images and the corresponding H&E images are depicted in Figures 6A and 6B. A great similarity can be observed between the proposed method and conventional pathological examinations. Figure 6A presents the adipocytes, while Figure 6B shows the tumor region and a significant stromal reaction. In Figures 6C and 6D, two clusters of tumor cell nuclei (indicated by red and blue solid boxes in Figure 6B) are magnified with the corresponding pseudo-colorized DRUM and H&E images. Although cell nuclei are loosely distributed, they have variable sizes and irregular shapes, which are used to diagnose tumor cells. These results suggest that DRUM can not only visualize breast tissues with sufficient image contrast but also enable the differentiation of tumor cell nuclei and lymphocyte cell nuclei due to its high resolution.

High signal-to-background ratio imaging of cell nuclei by dark-field reflectance ultraviolet microscopy

Cell nuclei are important diagnostic features; thus, the SBR was used to quantitatively evaluate the visibility of cell nuclei by DRUM imaging. For normal mouse brain tissues, the same areas of freshly excised and thick samples were captured with different filter channels to obtain DRUM images (I_{260}) and autofluorescence images (I_{357}). Subsequently, the thick sample was labeled with DAPI, and the same area was imaged under a 447-nm filter channel (I_{447}). For the tumor tissues in Figures 4, 5, and 6, only DRUM images and autofluorescence images from the same areas were compared. Because these tissues are rare, they were processed

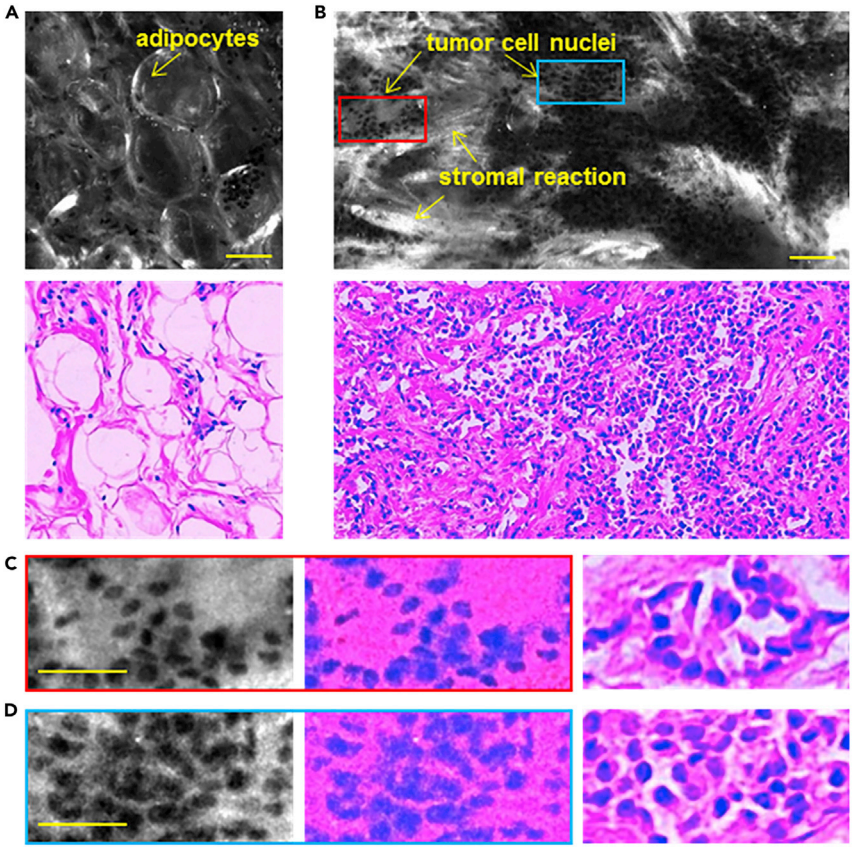

Figure 6. DRUM and pseudo-colorized DRUM validation of surgically excised, cryopreserved, and thick human breast cancer tissues

(A and B) DRUM images with the corresponding H&E images.

(C and D) Zoomed-in DRUM images (left) of red and blue solid regions in (B), with the corresponding pseudo-colorized DRUM images (middle) and H&E images (right). The contrast of DRUM images was adjusted in Fiji. Scale bars: 100 μm (A and B), 30 μm (C and D).

using a standard histological procedure to obtain H&E images. Figure 7A presents the comparison results for the hippocampus and internal capsule of normal mouse brain tissues, while Figures 7B–7D compare the DRUM and autofluorescence images of thick and label-free tumor tissues. In addition, a comparison of the intensity profiles of the cross-sections (red lines in I_{260}, green lines in I_{357}, and blue lines in I_{447}) is plotted in the right column. The negative contrast in both the DRUM and autofluorescence images was inverted into a positive contrast. The visibility of cell nuclei by DRUM is much more significant than that of autofluorescence images and close to the degree of DAPI-labeled images. In particular, some cell nuclei in tumor tissues that cannot be resolved by UV-based autofluorescence imaging are still distinguishable by DRUM (Figures 7B and 7D). Because in these tissues, the autofluorescence signal is weaker than the reflected signal, leading to lower positive signal caused by extranuclear components in I_{357}. As shown in Figure 7E, the statistical SBRs of five cell nuclei were calculated. The results suggest that, compared to autofluorescence images, the SBR by DRUM can be improved by a factor of ~ two in the hippocampus and ~ three in the internal capsule. Compared with the hippocampus, known as gray matter regions, the internal capsule, where nerve fibers are distributed and are known as white matter regions, has higher RI and provides stronger positive contrast, leading to a higher SBR improvement. Furthermore, the SBR of DRUM imaging in tumor tissues was lower than that in normal tissues. It is suspected that tumor cells affect the extranuclear components and decrease reflection signals.

DISCUSSION

In this study, we proposed and implemented DRUM and pseudo-colorized DRUM for the rapid and high-SBR imaging of unprocessed, thick, and label-free tissues. The superiority of the DRUM is as follows: First, to the

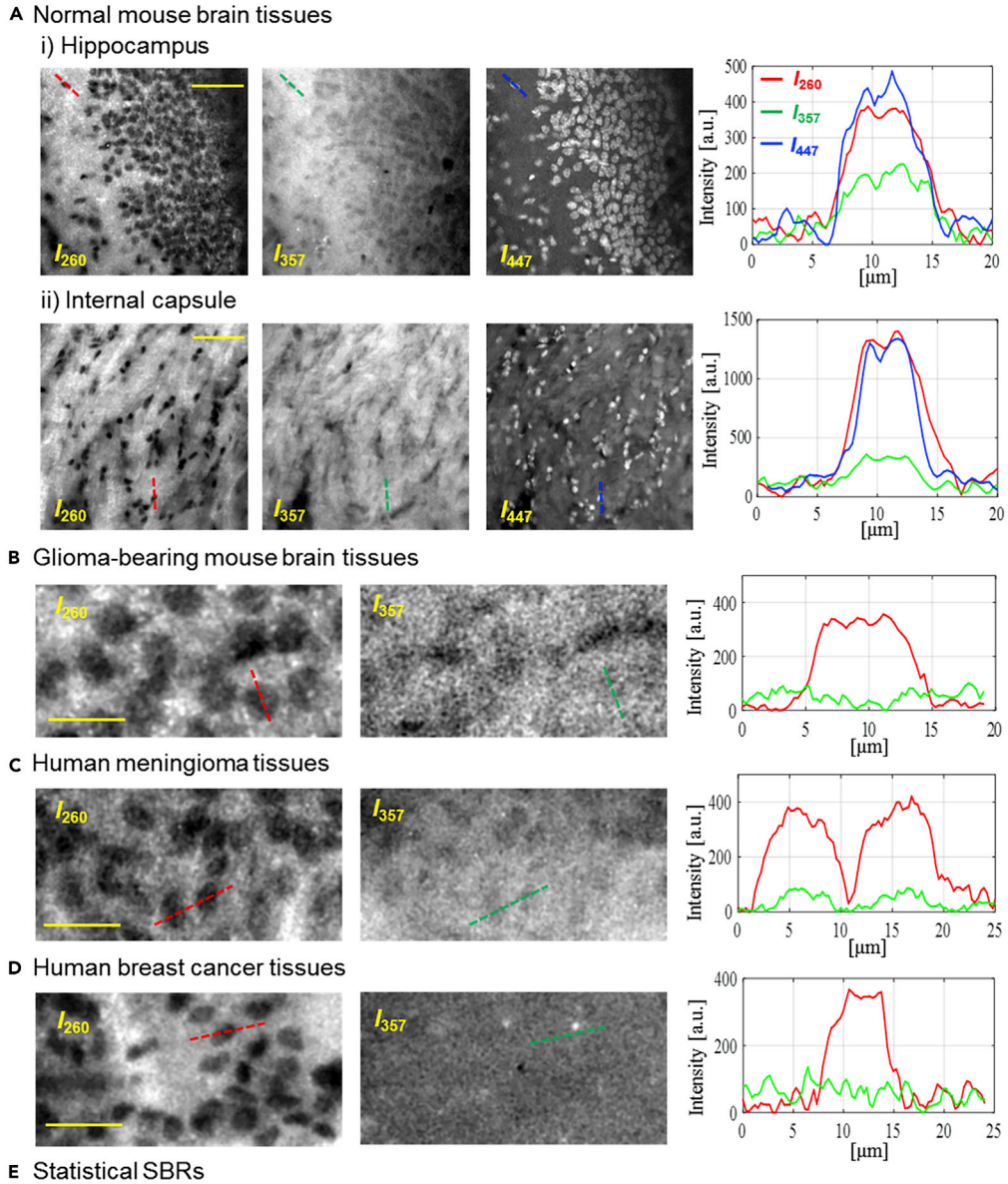

E Statistical SBRs

	I_{260}	I_{357}	I_{447}
Hippocampus	9.2 ± 0.2	4.3 ± 0.3	9.7 ± 0.2
Internal capsule	12.7 ± 0.2	4.0 ± 0.2	13.4 ± 0.2
Glioma-bearing mouse brain tissues	7.5 ± 0.2	2.3 ± 0.6	/
Human meningioma tissues	7.1 ± 0.5	2.7 ± 0.5	/
Human breast cancer tissues	8.0 ± 0.3	/	/

Figure 7. High SBR imaging of cell nuclei by DRUM

(A) Comparison of normal mouse brain tissues between DRUM image (I_{260}), autofluorescence image (I_{357}), and DAPI-labeled fluorescence image (I_{447}).

(B–D) Comparison between DRUM image (I_{260}) and autofluorescence image (I_{357}) in glioma-bearing mouse brain tissues, human brain-tumor tissues, and human breast cancer tissues.

(E) Statistical SBRs of ten cell nuclei from (A–D). Scale bars: 50 μm (A), 20 μm (B–D). Data are represented as mean ± Standard Deviation.

best of our knowledge, DRUM can provide imaging results for pathological assessment with the shortest turnaround time. For sample preparation, thick and unprocessed tissues were used without labeling the exogenous fluorophores and without laborious steps for the physical section. For tissue imaging, the DRUM setup in a wide-field configuration enables parallel pixel acquisition and no complex mathematical reconstruction is required. Overall, the turnaround time from sample preparation to DRUM image acquisition is only 2-3 min, thus DRUM is well suited for intraoperative histopathology. Second, DRUM images have subcellular resolution and a high SBR. By fully utilizing the advantage of the short wavelength of deep-UV light, DRUM can individually resolve cell nuclei, even densely packed cell nuclei in the hippocampus and tumor regions (e.g., Figures 3C and 4E). More importantly, the visibility of cell nuclei provided by DRUM is much more significant than that of autofluorescence images and close to the degree of DAPI-labeled images. In particular, some cell nuclei in tumor tissues that could not be resolved by UV-based autofluorescence imaging were distinguishable by DRUM (Figures 7B and 7D). Finally, the DRUM setup is simple and cost-effective, which makes it possible to enter the operating room for intraoperative histopathology, and is accepted by cost-sensitive pathologists (Details on comparison between DRUM and other histological imaging methods can be found in Figure S2).

Rapid and accurate intraoperative tissue imaging is essential, which can help surgeons or pathologists interpret and decrease the surgical risk. Undoubtedly, DRUM and pseudo-colorized DRUM can serve as additional intraoperative aids. The purpose of the proposed method is not to replace conventional histological examinations, but rather to complement them. Intraoperatively excised tissues can be immediately imaged by DRUM within 2-3 min, to determine the presence of suspicious tissue. Subsequently, owing to the non-destructive property of DRUM, the tissues can be further processed by conventional histological examination to obtain a full diagnosis. Furthermore, the proposed method is still in an early stage of development, and the practicality of DRUM and pseudo-colorized DRUM can be further improved for clinical translation. First, multispectral deep UV light can be used to provide more information about extranuclear components.[48–50] Then, the development of deep-learning algorithms may avoid the use of autofluorescence images and directly convert DRUM images into an authentic H&E appearance with high accuracy. Furthermore, the imaging performance of different tissues and their applications in clinical settings should be further investigated.

In summary, DRUM is a transformative and promising histological imaging method that enables rapid and non-destructive imaging of unprocessed, thick, and label-free tissues with subcellular resolution and high SBR. Using the proposed method, cell nuclei and some tissue architectures can be resolved in normal mouse tissues, and tumor cells can be identified in glioma-bearing mouse brain tissues, human brain tumor tissues, and human breast cancer tissues. We believe that the proposed method has the potential to detect and distinguish normal and cancer cells in a clinical setting and to aid intraoperative assessment, including brain tumor surgery and breast-conserving surgery.

Limitations of the study

DRUM and pseudo-colorized DRUM have some limitations. First, the visibility of nucleoli structures is more significant in H&E-stained images than in DRUM (Figures 3C–3F). Likely, the image contrast of nucleoli provided by DRUM is not identical to that in the H&E histological images. Second, the depth-of-field (DOF) of the existing DRUM setup cannot completely accommodate various surface irregularities and causes slight out-of-focus blurs (the extended-FOV DRUM images in Figures 3, 4, 5, and 6). This problem can be solved using extended DOF technologies, such as the collection of a sequence of axially refocused images or a combination of wavefront coding and digital recovery.[51] Finally, although pseudo-colorized DRUM enhances image familiarity of pathologists, it is less effective in preserving the cell nuclei structures in tumor tissues than in normal tissues (Figures 6C and 6D). This is a limitation of the current virtual staining process that requires high image contrast.

STAR★METHODS

Detailed methods are provided in the online version of this paper and include the following:

- KEY RESOURCES TABLE
- RESOURCE AVAILABILITY
  - Lead contact
  - Materials availability
  - Data and code availability

SUPPLEMENTAL INFORMATION

Supplemental information can be found online at https://doi.org/10.1016/j.isci.2022.105849.

ACKNOWLEDGMENTS

This work was supported by the National Key Research and Development Program of China (2017YFC0110200), the National Natural Science Foundation of China (91959121, 82071972, 62105353, 92159104), the Natural Science Foundation of Guangdong Province (2020B121201010, 2021A1515012022), the Scientific Instrument Innovation Team of the Chinese Academy of Sciences (GJJSTD20180002), and the Shenzhen Basic Research Program (RCJC20200714114433058, RCYX20210609104445093, ZDSY20130401165820357), SIAT Innovation Program for Excellent Young Researchers (E1G029).

AUTHOR CONTRIBUTIONS

S. Y. and W. Z. conceived the study. S. Y., C. H., and J. Y. built the imaging system. J. Z., F. X., N. Wang, P. L., X. M., and P. G. prepared the specimens involved in this study. S. Y. performed imaging experiments. J. Z. and L. N. performed frozen section and histological staining. S. Y., Y. H., and H. L. processed and analyzed the data. Z. W. and P. G. performed pathological diagnosis on tumor tissues. S. Y. and W. Z. wrote the article. W. Z. supervised the whole study.

DECLARATION OF INTERESTS

S. Ye, H. Li, and W. Zheng have applied for patents (Chinese Patent Application No.: CN202211224969.8 and CN202222637881.0) related to the work reported in this article.

Received: September 14, 2022
Revised: December 4, 2022
Accepted: December 19, 2022
Published: January 20, 2023

REFERENCES

1. Somerset, H.L., and Kleinschmidt-DeMasters, B.K. (2011). Approach to the intraoperative consultation for neurosurgical specimens. Adv. Anat. Pathol. *18*, 446–449.
2. Preeti, A., Sameer, G., Kulranjan, S., Arun Abhinav, S., Preeti, R., Sunita, Y., and Madhu Mati, G. (2016). Intra-operative frozen sections: experience at A tertiary Care centre. Asian Pac. J. Cancer Prev. *17*, 5057–5061.
3. Fereidouni, F., Harmany, Z.T., Tian, M., Todd, A., Kintner, J.A., McPherson, J.D., Borowsky, A.D., Bishop, J., Lechpammer, M., Demos, S.G., and Levenson, R. (2017). Microscopy with ultraviolet surface excitation for rapid slide-free histology. Nat. Biomed. Eng. *1*, 957–966.
4. Chen, Z., Yu, W., Wong, I.H.M., and Wong, T.T.W. (2021). Deep-learning-assisted microscopy with ultraviolet surface excitation for rapid slide-free histological imaging. Biomed. Opt Express *12*, 5920–5938.
5. Yoshitake, T., Giacomelli, M.G., Quintana, L.M., Vardeh, H., Cahill, L.C., Faulkner-Jones, B.E., Connolly, J.L., Do, D., and Fujimoto, J.G. (2018). Rapid histopathological imaging of skin and breast cancer surgical specimens using immersion microscopy with ultraviolet surface excitation. Sci. Rep. *8*, 4476.
6. Schlichenmeyer, T.C., Wang, M., Elfer, K.N., and Brown, J.Q. (2014). Video-rate structured illumination microscopy for high-throughput imaging of large tissue areas. Biomed. Opt Express *5*, 366–377.
7. Zhang, Y., Kang, L., Lo, C.T.K., Tsang, V.T.C., and Wong, T.T.W. (2022). Rapid slide-free and non-destructive histological imaging using wide-field optical-sectioning microscopy. Biomed. Opt Express *13*, 2782–2796.
8. Wang, M., Kimbrell, H.Z., Sholl, A.B., Tulman, D.B., Elfer, K.N., Schlichenmeyer, T.C., Lee, B.R., Lacey, M., and Brown, J.Q. (2015). High-resolution rapid diagnostic imaging of whole prostate biopsies using video-rate fluorescence structured illumination microscopy. Cancer Res. *75*, 4032–4041.
9. Glaser, A.K., Reder, N.P., Chen, Y., McCarty, E.F., Yin, C., Wei, L., Wang, Y., True, L.D., and Liu, J.T.C. (2017). Light-sheet microscopy for slide-free non-destructive pathology of large clinical specimens. Nat. Biomed. Eng. *1*, 0084.
10. Glaser, A.K., Reder, N.P., Chen, Y., Yin, C., Wei, L., Kang, S., Barner, L.A., Xie, W., McCarty, E.F., Mao, C., et al. (2019). Multi-immersion open-top lightsheet microscope for high-throughput imaging of cleared tissues. Nat. Commun. *10*, 2781–2788.
11. Xie, W., Glaser, A.K., Vakar-Lopez, F., Wright, J.L., Reder, N.P., Liu, J.T.C., and True, L.D. (2020). Diagnosing 12 prostate needle cores within an hour of biopsy via open-top light-sheet microscopy. J. Biomed. Opt. *25*, 126502.
12. Chen, Y., Xie, W., Glaser, A.K., Reder, N.P., Mao, C., Dintzis, S.M., Vaughan, J.C., and Liu,

J.T.C. (2019). Rapid pathology of lumpectomy margins with open-top light-sheet (OTLS) microscopy. Biomed. Opt Express *10*, 1257–1272.

13. Que, S.K.T., Fraga-Braghiroli, N., Grant-Kels, J.M., Rabinovitz, H.S., Oliviero, M., and Scope, A. (2015). Through the looking glass: basics and principles of reflectance confocal microscopy. J. Am. Acad. Dermatol. *73*, 276–284.

14. Navarrete-Dechent, C., Cordova, M., Liopyris, K., Rishpon, A., Aleissa, S., Rossi, A.M., Lee, E., Chen, C.C.J., Busam, K.J., Marghoob, A.A., and Nehal, K.S. (2020). Reflectance confocal microscopy and dermoscopy aid in evaluating repigmentation within or adjacent to lentigo maligna melanoma surgical scars. J. Eur. Acad. Dermatol. Venereol. *34*, 74–81.

15. Yin, C., Wei, L., Abeytunge, S., Peterson, G., Rajadhyaksha, M., and Liu, J. (2019). Label-free in vivo pathology of human epithelia with a high-speed handheld dual-axis confocal microscope. J. Biomed. Opt. *24*, 030501.

16. Wong, T.T.W., Zhang, R., Hai, P., Zhang, C., Pleitez, M.A., Aft, R.L., Novack, D.V., and Wang, L.V. (2017). Fast label-free multilayered histology-like imaging of human breast cancer by photoacoustic microscopy. Sci. Adv. *3*, e1602168.

17. Liu, X., Wong, T.T.W., Shi, J., Ma, J., Yang, Q., and Wang, L.V. (2018). Label-free cell nuclear imaging by Gruneisen relaxation photoacoustic microscopy. Opt. Lett. *43*, 947–950.

18. Lai, P., Nie, L., and Wang, L. (2021). Special issue "Photoacoustic imaging: microscopy, tomography, and their recent applications in biomedicine" in visual computation for industry, biomedicine, and art. Vis. Comput. Ind. Biomed. Art *4*, 16.

19. Zhang, Y., Kang, L., Wong, I.H.M., Dai, W., Li, X., Chan, R.C.K., Hsin, M.K.Y., and Wong, T.T.W. (2022). High-throughput, label-free and slide-free histological imaging by computational microscopy and unsupervised learning. Adv. Sci. *9*, 2102358.

20. Skala, M.C., Riching, K.M., Gendron-Fitzpatrick, A., Eickhoff, J., Eliceiri, K.W., White, J.G., and Ramanujam, N. (2007). In vivo multiphoton microscopy of NADH and FAD redox states, fluorescence lifetimes, and cellular morphology in precancerous epithelia. Proc. Natl. Acad. Sci. USA *104*, 19494–19499.

21. Li, X., Li, H., He, X., Chen, T., Xia, X., Yang, C., and Zheng, W. (2018). Spectrum- and time-resolved endogenous multiphoton signals reveal quantitative differentiation of premalignant and malignant gastric mucosa. Biomed. Opt Express *9*, 453–471.

22. Chen, X., Nadiarynkh, O., Plotnikov, S., and Campagnola, P.J. (2012). Second harmonic generation microscopy for quantitative analysis of collagen fibrillar structure. Nat. Protoc. *7*, 654–669.

23. Tao, Y.K., Shen, D., Sheikine, Y., Ahsen, O.O., Wang, H.H., Schmolze, D.B., Johnson, N.B., Brooker, J.S., Cable, A.E., Connolly, J.L., and Fujimoto, J.G. (2014). Assessment of breast pathologies using nonlinear microscopy. Proc. Natl. Acad. Sci. USA *111*, 15304–15309.

24. Weigelin, B., Bakker, G.J., and Friedl, P. (2016). Third harmonic generation microscopy of cells and tissue organization. J. Cell Sci. *129*, 245–255.

25. Sun, Y., You, S., Tu, H., Spillman, D.R., Jr., Chaney, E.J., Marjanovic, M., Li, J., Barkalifa, R., Wang, J., Higham, A.M., et al. (2018). Intraoperative visualization of the tumor microenvironment and quantification of extracellular vesicles by label-free nonlinear imaging. Sci. Adv. *4*, eaau5603.

26. Freudiger, C.W., Min, W., Saar, B.G., Lu, S., Holtom, G.R., He, C., Tsai, J.C., Kang, J.X., and Xie, X.S. (2008). Label-free biomedical imaging with high sensitivity by stimulated Raman scattering microscopy. Science *322*, 1857–1861.

27. Liu, Z., Su, W., Ao, J., Wang, M., Jiang, Q., He, J., Gao, H., Lei, S., Nie, J., Yan, X., et al. (2022). Instant diagnosis of gastroscopic biopsy via deep-learned single-shot femtosecond stimulated Raman histology. Nat. Commun. *13*, 4050.

28. Orringer, D.A., Pandian, B., Niknafs, Y.S., Hollon, T.C., Boyle, J., Lewis, S., Garrard, M., Hervey-Jumper, S.L., Garton, H.J.L., Maher, C.O., et al. (2017). Rapid intraoperative histology of unprocessed surgical specimens via fibre-laser-based stimulated Raman scattering microscopy. Nat. Biomed. Eng. *1*, 0027.

29. Beaurepaire, E., Boccara, A.C., Lebec, M., Blanchot, L., and Saint-Jalmes, H. (1998). Full-field optical coherence microscopy. Opt. Lett. *23*, 244–246.

30. Dubois, A., Vabre, L., Boccara, A.C., and Beaurepaire, E. (2002). High-resolution full-field optical coherence tomography with a Linnik microscope. Appl. Opt. *41*, 805–812.

31. Assayag, O., Grieve, K., Devaux, B., Harms, F., Pallud, J., Chretien, F., Boccara, C., and Varlet, P. (2013). Imaging of non-tumorous and tumorous human brain tissues with full-field optical coherence tomography. Neuroimage. Clin. *2*, 549–557.

32. Kumamoto, Y., Taguchi, A., and Kawata, S. (2019). Deep-ultraviolet biomolecular imaging and analysis. Adv. Opt. Mater. *7*, 1801099.

33. Zeskind, B.J., Jordan, C.D., Timp, W., Trapani, L., Waller, G., Horodincu, V., Ehrlich, D.J., and Matsudaira, P. (2007). Nucleic acid and protein mass mapping by live-cell deep-ultraviolet microscopy. Nat. Methods *4*, 567–569.

34. Ojaghi, A., Carrazana, G., Caruso, C., Abbas, A., Myers, D.R., Lam, W.A., and Robles, F.E. (2020). Label-free hematology analysis using deep-ultraviolet microscopy. Proc. Natl. Acad. Sci. USA *117*, 14779–14789.

35. Giannios, P., Toutouzas, K.G., Matiatou, M., Stasinos, K., Konstadoulakis, M.M., Zografos, G.C., and Moutzouris, K. (2016). Visible to near-infrared refractive properties of freshly-excised human-liver tissues: marking hepatic malignancies. Sci. Rep. *6*, 27910.

36. Menzel, M., Axer, M., Amunts, K., De Raedt, H., and Michielsen, K. (2019). Diattenuation Imaging reveals diferent brain tissue properties. Sci. Rep. *9*, 1939.

37. van Ginneken, B., Stavridi, M., and Koenderink, J.J. (1998). Diffuse and specular reflectance from rough surfaces. Appl. Opt. *37*, 130–139.

38. Wolff, L.B. (1994). Diffuse-reflectance model for smooth dielectric surfaces. J. Opt. Soc. Am. A *11*, 2956–2968.

39. Khan, R., Gul, B., Khan, S., Nisar, H., and Ahmad, I. (2021). Refractive index of biological tissues: Review, measurement techniques, and applications. Photodiagnosis Photodyn. Ther. *33*, 102192.

40. Li, C., Pitsillides, C., Runnels, J.M., Côté, D., and Lin, C.P. (2010). Multiphoton microscopy of live tissues with ultraviolet autofluorescence. IEEE J. Sel. Top. Quant. Electron. *16*, 516–523.

41. Sun, J., Lee, S.J., Wu, L., Sarntinoranont, M., and Xie, H. (2012). Refractive index measurement of acute rat brain tissue slices using optical coherence tomography. Opt Express *20*, 1084–1095.

42. Sanai, N., Polley, M.Y., McDermott, M.W., Parsa, A.T., and Berger, M.S. (2011). An extent of resection threshold for newly diagnosed glioblastomas. J. Neurosurg. *115*, 3–8.

43. Renner, D.N., Jin, F., Litterman, A.J., Balgeman, A.J., Hanson, L.M., Gamez, J.D., Chae, M., Carlson, B.L., Sarkaria, J.N., Parney, I.F., et al. (2015). Effective treatment of established GL261 murine gliomas through picornavirus vaccination-enhanced tumor antigen-specific CD8+ T Cell Responses. PLoS One *10*, e0125565.

44. Schindelin, J., Arganda-Carreras, I., Frise, E., Kaynig, V., Longair, M., Pietzsch, T., Preibisch, S., Rueden, C., Saalfeld, S., Schmid, B., et al. (2012). Fiji: an open-source platform for biological-image analysis. Nat. Methods *9*, 676–682.

45. Arganda-Carreras, I., Kaynig, V., Rueden, C., Eliceiri, K.W., Schindelin, J., Cardona, A., and Sebastian Seung, H. (2017). Trainable Weka Segmentation: a machine learning tool for microscopy pixel classification. Bioinformatics *33*, 2424–2426.

46. Kobbermann, A., Unzeitig, A., Xie, X.J., Yan, J., Euhus, D., Peng, Y., Sarode, V., Moldrem, A., Marilyn Leitch, A., Andrews, V., et al. (2011). Impact of routine cavity shave margins on breast cancer re-excision rates. Ann. Surg Oncol. *18*, 1349–1355.

47. Jung, W., Kang, E., Kim, S.M., Kim, D., Hwang, Y., Sun, Y., Yom, C.K., and Kim, S.W. (2012). Factors associated with re-excision after breast-conserving surgery for early-stage breast cancer. J. Breast Cancer *15*, 412–419.

48. Yao, D.K., Chen, R., Maslov, K., Zhou, Q., and Wang, L.V. (2012). Optimal ultraviolet wavelength for *in vivo* photoacoustic imaging of cell nuclei. J. Biomed. Opt. *17*, 056004.

49. Soltani, S., Ojaghi, A., and Robles, F.E. (2019). Deep UV dispersion and absorption spectroscopy of biomolecules. Biomed. Opt Express *10*, 487–499.

50. Ojaghi, A., Fay, M.E., Lam, W.A., and Robles, F.E. (2018). Ultraviolet hyperspectral interferometric microscopy. Sci. Rep. *8*, 9913.

51. Zammit, P., Harvey, A.R., and Carles, G. (2014). Extended depth-of-field imaging and ranging in a snapshot. Optica *1*, 209–216.

52. Ruifrok, A.C., and Johnston, D.A. (2001). Quantification of histochemical staining by color deconvolution. Anal. Quant. Cytol. Histol. *23*, 291–299.

53. Torres, R., Vesuna, S., and Levene, M.J. (2014). High-resolution, 2- and 3-dimensional imaging of uncut, unembedded tissue biopsy samples. Arch. Pathol. Lab Med. *138*, 395–402.

STAR★METHODS

KEY RESOURCES TABLE

REAGENT or RESOURCE	SOURCE	IDENTIFIER
Bilogical samples		
Normal mouse brain and slpeen tissue	This paper	N/A
GL261 tumor-bearing mouse brain tissues	This paper	N/A
Human brain-tumor tissues.	Sun Yat-Sen Memorial Hospital	N/A
Human breast cancer tissues.	Shenzhen University General Hospital	N/A
Software and algorithms		
Matlab	Mathworks Inc.	2016b
Fiji[44]	Schindelin et al., 2012	https://imagej.net/software/fiji/
GraphPad Prism	GraphPad Software	Version 9
Trainable Weka segmentation[45]	Arganda-Carreras et al., 2017	https://doi.org/10.1093/bioinformatics/btx180
Other		
UV LED	LED TaoYuan	TY-UVCLED-265
Biconvex lens	Heng Yang Guang Xue	GLH22-025-025-UV
Plano-convex lens	Heng Yang Guang Xue	GLH21-025-050-UV
UV filter	Semrock	FF01-260/16–25
Other filters	Edmund Optics	86981, 84095
Objective	Sigmakoki	PFL-20-UV/NUV-AG-A,
Tube lens	Sigmakoki	TL-Y4
UV sCMOS camera	Tucsen	Dhyana 400BSI
3-axis motorized stage	Thorlabs	MTS25/M-Z8
Freezing microtome	Leica	CM1950

RESOURCE AVAILABILITY

Lead contact

Further information and requests for reagents and resources should be directed to and will be fulfilled by the lead contact, Wei Zheng (zhengwei@siat.ac.cn).

Materials availability

This study did not generate new unique reagents.

Data and code availability

- Data reported in this paper will be shared by the lead contact upon request.
- Matlab codes are available from the lead contact upon request.
- Any additional data supporting findings on this study are available from the lead contact upon request.

METHOD DETAILS

Collection of animal and human tissues

Animal organs were extracted from C57BL/6J mice. For frozen mice tissues (Figure 2), mice were deeply anesthetized, perfused transcardially using PBS, and then fixed using 4% paraformaldehyde. Immediately thereafter, the brains were dissected and fixed in 4% paraformaldehyde for 24 h. Next, the brain was dehydrated in a gradient sucrose solution (20% and 40%) until it sank to the bottom. Finally, the brain was cut into 10-μm frozen sections using a freezing microtome (Leica, CM1950). For fresh mouse tissues (Figures 3,

4, and 7), the brain and spleen were harvested immediately after the mice were sacrificed and manually sectioned at ~1.5-mm thickness, and then rinsed in PBS for several seconds.

For human brain tumor tissues, formalin-fixed specimens from patients diagnosed with meningiomas (Figures 5 and 7) and pilocytic astrocytoma (Figure S1) were collected with the approval of Sun Yat-Sen Memorial Hospital. For human breast cancer tissues (Figures 6 and 7), specimens were cut from patients who underwent breast-conserving surgery. The tissues were stored at −80°C and transported to the laboratory for imaging, with the approval of the Institutional Review Board at Shenzhen University General Hospital. Before DRUM imaging, both the human brain and breast tissues were manually sectioned (~1.5-mm thickness), then rinsed in PBS for several seconds.

For all tissues to be imaged by DRUM, we slowly dropped PBS or glycerin on the tissue surface using a pipette to avoid bubbles. Subsequently, a cover glass was sealed on the tissue surface to ensure that the space between the cover glass and tissue surface was filled with PBS or glycerin without any bubbles. It is noted that all the slide glasses and cover glasses are made of fused silica, which has a transmittance of over 90% for wavelengths ranging from 220 to 700 nm.

After DRUM imaging, all tissues were processed using the standard histological procedure to obtain H&E-stained images. All animal experiments were performed in compliance with the protocols approved by the Guangdong Provincial Animal Care and Use Committee and the guidelines of the Animal Experimentation Ethics Committee of Shenzhen Institutes of Advanced Technology, Chinese Academy of Sciences.

Glioma mouse model

For tumor implantation, GL261 murine glioma cells were trypsinized with 0.05% trypsin–EDTA, washed, and resuspended in PBS at a final concentration of 3×10^5 cells/μL. Six-to eight-week-old C57BL/6J mice were used to establish orthotopic glioma. Anesthetized mice were stereotactically injected into the right striatum with 6×10^5 GL261 cells in a total volume of 2-μL μL physiologic saline at a rate of 0.2 μL/min. The injection coordinates were 1 mm anterior, and 1.5 mm lateral to the bregma, at a depth of 3 mm from the cortical surface. Finally, the injection holes were sealed with dental cement, and the cut skin of the head was sutured.

Optical setup

As shown in Figure 1F, light from one or more UV LEDs (TY-UVCLED-265, LED TaoYuan) was collected using a biconvex lens (f_1 = 25 mm) and filtered using a UV filter (FF01-260/16–25, Semrock). The oblique beam was then focused onto the tissue using a short-focal-length plano-convex lens (f_2 = 50 mm). The light intensity on the sample plane was measured to be 20 mW per LED, with an illuminating area of approximately 5 mm^2. For imaging, we used a 20× UV microscope objective (PFL-20-UV/NUV-AG-A, NA = 0.36, Sigmakoki) and corresponding tube lens (TL-Y4, Sigmakoki). Band-pass filters (FF01-260/16–25, Semrock; 86981, 84095, Edmund Optics) installed on a filter wheel were inserted and allowed for light transmission in three wavelength regions centered at 260, 357, and 447 nm. Finally, images were recorded using a UV sCMOS camera (Dhyana 400BSI, Tucsen). The acquisition time for each raw image was set to ~300 ms to balance the image signal-to-noise ratio (SNR) and acquisition speed.

The field of view (FOV) of each image was ~600 × 600 μm^2. For extended FOV imaging, 2D raster scanning by a high-precision 2-axis motorized stage (MTS25/M-Z8, Thorlabs) was implemented to obtain a sequence of DRUM images with overlaps (20% FOV). The overlapped and organized images were then stitched using the Fiji plugin (Grid/Collection stitching).

Image processing and virtual staining of DRUM images

To remove artifacts from non-uniform illumination, the collected images were normalized to a reference background image acquired from a blank area on the sample for each wavelength. Then, as shown in Figure 1G, the process of pseudo-colorized DRUM includes the following steps[52,53]: i) The DRUM images (I_{260}) were directly inverted by the inverse function of the Fiji software. ii) The intensity values from autofluorescence (I_{357}) and inverted DRUM images (I_{inv_260}) were converted to optical densities in the red, green, and blue channels according to the published matrix values for H&E. Autofluorescence intensity was assigned to the eosin channel, whereas the positive signal of cell nuclei from inverted DRUM images was assigned to the hematoxylin channel. Following image normalization and scaling to achieve adequate contrast, the red

(*R*), green (*G*), and blue (*B*) channel values for the pseudo-colorized DRUM images were calculated as follows:

$$\begin{aligned} R &= 10^{-\left(0.644 I_{357} + 0.093 I_{inv\_260}\right)} \\ G &= 10^{-\left(0.717 I_{357} + 0.954 I_{inv\_260}\right)} \\ B &= 10^{-\left(0.267 I_{357} + 0.283 I_{inv\_260}\right)} \end{aligned} \quad \text{(Equation 1)}$$

QUANTIFICATION AND STATISTICAL ANALYSIS

To calculate the cross-sectional area and intercellular distance of cell nuclei in Figure 4, DRUM images were segmented using a Fiji plugin (trainable Weka segmentation[45]) and subsequently converted to a binary image where cell nuclei can be identified. Then, the binarized DRUM images were analyzed in Fiji. The cross-sectional area can be directly provided, and the intercellular distance is calculated as the shortest adjacent distance to a neighboring cell nucleus based on the localized center positions of cell nuclei. Finally, a two-tailed paired *t* test was carried out across groups with $N = 50$ for each distribution of cross-sectional area and intercellular distance. No assumptions were made on data distributions. The significance was defined as $p < 0.05$. Statistical analysis was carried out using GraphPad Prism software (GraphPad Software).